



Evidence for a Delayed Progenitor Population for CHIME non-repeating Fast Radio Bursts using a Self-Consistent Forward and Backward Inference Framework

ZI-LIANG ZHANG (张子良) ^{1,2} AND BING ZHANG (张冰) ^{1,2}

¹*The Hong Kong Institute for Astronomy and Astrophysics (HKIAA), The University of Hong Kong, Pokfulam Road, Hong Kong, People's Republic of China*

²*Department of Physics, The University of Hong Kong, Pokfulam Road, Hong Kong, People's Republic of China*

ABSTRACT

Fast radio bursts (FRBs) are luminous extragalactic radio transients whose physical origins remain uncertain. Using over one thousand non-repeating events from CHIME/FRB Catalog 2, we infer the intrinsic FRB demographics with a self-consistent framework that combines backward non-parametric inference and forward population synthesis while accounting for probabilistic dispersion measure–redshift estimates, baseband-to-catalog fluence corrections, and the latest fuzzy multidimensional selection function. We first apply a backward non-parametric method, the weighted Lynden–Bell C^- estimator, to recover the intrinsic redshift and energy distributions without assuming any population model. Independently, we perform forward Monte Carlo population synthesis in observable dispersion measure–fluence space, treating candidate intrinsic redshift and energy distributions as population hypotheses and comparing the resulting selected synthetic catalogs with observations. We find that the intrinsic redshift distribution peaks at $z \sim 1$, significantly lower than the cosmic star formation history (SFH) peak at $z \sim 1.7$, indicating clear tension with a pure SFH-tracking scenario, suggesting that at least some FRBs are delayed with respect to SFH. The intrinsic energy distribution is consistent with a power law of index $\alpha \approx 1.9$ and steepens at higher energies. We find no significant evidence for a redshift–energy distribution correlation.

Keywords: Radio bursts (1339); Radio transient sources (2008)

1. INTRODUCTION

Fast radio bursts (FRBs) are short and intense radio transients with unknown progenitors (D. R. Lorimer et al. 2007; D. Thornton et al. 2013; E. Petroff et al. 2022; B. Zhang 2023). The sources of the entire FRB population are not identified. The discovery of an X-ray burst associated with FRB 20200428A from the Galactic magnetar SGR 1935+2154 (e.g., C. D. Bochenek et al. 2020; CHIME/FRB Collaboration et al. 2020; C. K. Li et al. 2021), associated with a supernova remnant G57.02+0.8 (B. M. Gaensler 2014; R. Kothes et al. 2018; P. Zhou et al. 2020), points to a young environment. By contrast, FRB 20200120E, located in a globular cluster in M81, points to an old environment (F. Kirsten et al. 2022).

A population study of FRBs can help constrain intrinsic energy function and redshift distribution of FRBs, and the results are continuously updated as the FRB sample grows (e.g., Y.-W. Yu et al. 2014; M. Caleb et al. 2016; W. Lu & P. Kumar 2016; X.-F. Cao et al. 2018; R. Luo et al. 2018; W. Lu & A. L. Piro 2019; R. Luo

et al. 2020; R. C. Zhang et al. 2021; R. C. Zhang & B. Zhang 2022; T. Hashimoto et al. 2022; C. W. James et al. 2022a; K. Shin et al. 2023; Y. Wang & J. van Leeuwen 2024; O. Gupta et al. 2025). The well-localized events are most valuable for understanding the physical nature of FRBs, but the sample size of such precisely localized sources remains small (e.g., S. Chatterjee et al. 2017; V. Ravi et al. 2019; K. W. Bannister et al. 2019; B. Marcote et al. 2020; C.-H. Niu et al. 2022; L. N. Driessen et al. 2024). Also, in the past the FRB sources were detected using a diverse array of telescopes with different observing frequencies, sensitivities, and trigger criteria. The resulting combined sample is therefore deeply heterogeneous.

To overcome the limitations of both sample size and instrumental heterogeneity, the statistical properties of a broader, uniformly selected unlocalized population should be used. Specifically, the intrinsic redshift distribution can place stringent constraints on FRB progenitors. If the distribution tracks the cosmic star-formation history (SFH), it implies a young progenitor population, such as magnetars formed from core-collapse supernovae. Conversely, a distribution delayed relative to the SFH implies an older population, such as magnetars formed from binary white dwarf mergers, neutron

star mergers or accretion-induced white dwarf collapses. The energy function for non-repeating FRBs also reflects the global distribution of FRBs in energy among different sources, which carries the information of the FRB population in general.

The Canadian Hydrogen Intensity Mapping Experiment (CHIME) (CHIME/FRB Collaboration et al. 2018) provides exactly this type of homogeneous dataset. The number of detected FRBs increased by an order of magnitude in the first CHIME/FRB catalog (CHIME/FRB Collaboration et al. 2021) relative to earlier samples. However, despite the uniform instrumental origin of these bursts, the redshift and energy distributions inferred from this catalog using different statistical methods did not achieve full consensus. Through forward Monte Carlo simulations, R. C. Zhang & B. Zhang (2022) claimed that the FRB population is delayed with respect to the SFH. This conclusion was supported by several follow-up studies using various methods, including the V_{\max} method (T. Hashimoto et al. 2022), the forward modeling method (D.-C. Qiang et al. 2022; Z.-L. Zhang et al. 2023), the Lynden–Bell estimator without a fuzzy selection function (J. H. Chen et al. 2024; K. J. Zhang et al. 2025; S. Champati & V. Petrosian 2025), and forward fitting utilizing the baseband catalog (O. Gupta et al. 2025). On the other hand, a population analysis based on a weighting formalism with a more careful treatment of the instrumental selection effect (K. Shin et al. 2023) and a detailed forward population synthesis (Y. Wang & J. van Leeuwen 2024) concluded that the data are still consistent with FRBs tracking the SFH. Even though a delayed model may also be consistent with the data, it is not required.

Backward non-parametric methods provide a complementary route to FRB demographic inference because they recover the intrinsic redshift and energy distributions without imposing explicit parametric population models. In the Lynden–Bell C^- framework, they also provide a basis for testing whether redshift and energy can be treated as statistically independent population variables³ (D. Lynden-Bell 1971; B. Efron & V. Petrosian 1992). However, previous backward analyses generally did not include both the fuzzy CHIME/FRB selection function and the probabilistic nature of the $DM_{\text{ext}}-z$ relation (e.g., J. H. Chen et al. 2024; K. J. Zhang et al. 2025; S. Champati & V. Petrosian 2025). As emphasized by C. M. Bryant et al. (2021), replacing a gradual selection function with a sharp cutoff can bias the recovered intrinsic distributions and can induce apparent redshift–energy dependence. This issue is particularly relevant for CHIME/FRB, whose detection efficiency

strongly depends on multiple observables rather than on a single fluence threshold (CHIME/FRB Collaboration et al. 2021; M. Merryfield et al. 2023; K. McGregor et al. 2026). In addition, the catalog-reported fluence is generally a lower limit to the true fluence, which propagates directly into the inferred burst energy (CHIME/FRB Collaboration et al. 2021; B. C. Andersen et al. 2023; M. Merryfield et al. 2023; CHIME/FRB Collaboration et al. 2024).

CHIME/FRB Catalog 2 (CHIME/FRB Collaboration et al. 2026) contains more than 5000 events and provides a substantially larger sample for FRB population studies. In this work, we focus on non-repeating events and combine two complementary approaches that constrain the population from different directions, while explicitly propagating uncertainties associated with the $DM_{\text{ext}}-z$ relation and the catalog-reported fluences. We first convert the catalog fluences to baseband-like fluences. In the backward analysis, we apply the weighted Lynden–Bell C^- method to infer intrinsic population distributions, including the redshift distribution peak and the slope and high energy steepening of the energy distribution, and use Monte Carlo simulations to test redshift–energy independence. In the forward analysis, we perform Monte Carlo population synthesis as an independent population constraint in observable space: mock events generated from candidate intrinsic redshift and energy distributions are passed through the survey selection function and the $DM_{\text{ext}}(z)$ probability distribution (see Appendix A for the definition of DM_{ext}), and the resulting synthetic DM_{ext} and fluence distributions are compared directly with the observed distributions.

Figure 1 summarizes the analysis workflow. Section 2 describes the statistical frameworks for the weighted Lynden–Bell C^- inference and the forward population synthesis. Section 3 presents the inferred redshift and energy distributions, the redshift–energy independence tests, and the forward-modeling constraints. Section 4 summarizes the main conclusions.

2. METHOD

2.1. Sample selection

We take the CHIME Catalog 2 (CHIME/FRB Collaboration et al. 2026) and select a cleaner sample by excluding the following events:

1. events detected before 2018-09-04 (commissioning phase), as well as events flagged by *excluded_flag*, *citizen_science_flag*, or *sidelobe_flag*;
2. repeating bursts with a non-empty *repeater_name* field;
3. highly scattered events ($\tau > 10$ ms at 600 MHz), which are strongly affected by CHIME selection bias;

³ Here redshift–energy independence refers to the correlation of the intrinsic population distributions, not to the deterministic relation among fluence, luminosity distance, and isotropic-equivalent energy.

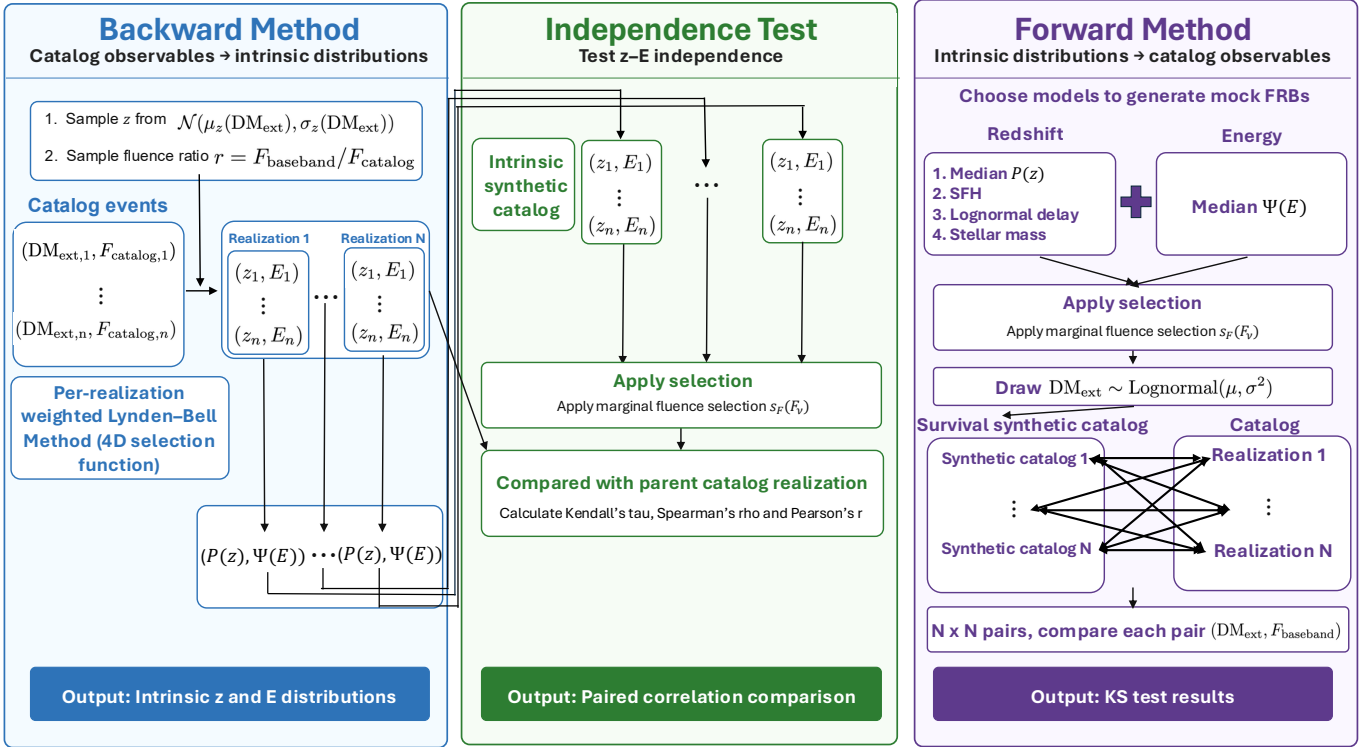


Figure 1. Flow chart summarizing the self-consistent backward-inference and forward-synthesis framework used in this work.

4. events with $\text{bonsai_snr} < 12$, to reduce incompleteness from human inspection near the low-S/N threshold;
5. events with $\text{dm_fitb} > 2000 \text{ pc cm}^{-3}$, where the selection function is not well constrained (see Figure 9 of M. Merryfield et al. (2023));
6. events with absolute meridian angle larger than 1° , where the pattern of baseband-to-catalog fluence ratio is different from events within 1° .

Criteria 1 through 4 represent standard quality and uniformity cuts commonly adopted in the literature (e.g., CHIME/FRB Collaboration et al. 2021; T. Hashimoto et al. 2022; K. Shin et al. 2023; CHIME/FRB Collaboration et al. 2026). Criterion 5 is explicitly introduced in this work to ensure the sample is strictly confined to the parameter space where the survey selection function is well defined and robustly calibrated against injection surveys. Criterion 6 is introduced to ensure a stable distribution of the baseband-to-catalog fluence ratio, see the next subsection for details. After applying these selection criteria, a sample of 1798 non-repeating FRBs is obtained for analysis.

2.2. Baseband fluence and selection function

The catalog-reported fluence generally provides only a lower limit to the burst physical fluence (B. C. Andersen et al. 2023; CHIME/FRB Collaboration et al. 2024, 2026). Correcting the catalog fluence is required because

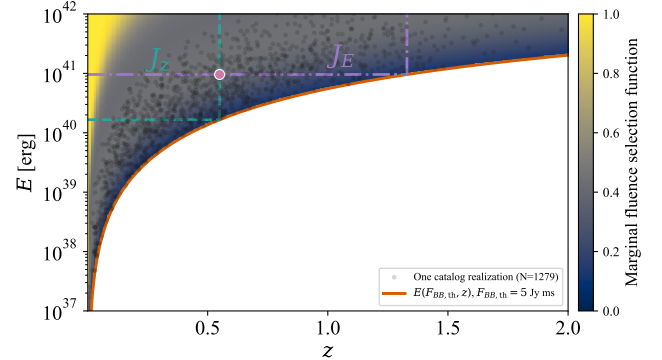


Figure 2. z - E distribution for the selected CHIME/FRB Catalog 2 sample. The black points show the catalog events, with the colorbar indicating the marginal fluence-only projection of the selection function. The red solid line represents the fluence-limited selection boundary at $F_{v,\text{th}} = 5 \text{ Jy ms}$, which is used to define the comparable sets in the weighted Lynden-Bell C^- method. The pink point (z_i, E_i) is used to illustrate the definition of the comparable sets J_{z_i} and J_{E_i} , which are defined by the green and purple dashed lines, respectively.

fluence enters directly into the energy estimate and the injection-based selection function (M. Merryfield et al. 2023; K. McGregor et al. 2026) is calibrated in terms of the injected physical fluence. Each catalog fluence is therefore converted to a baseband-like fluence by as-

signing a baseband-to-catalog fluence-ratio draw from the empirical distribution of [CHIME/FRB Collaboration et al. \(2024\)](#). The ratio spans a broad range, from values below unity to approximately 10^3 . Because the empirical ratio distribution remains stable for absolute meridian angle below 1° but changes systematically at larger meridian angles (see Figure 4 of [CHIME/FRB Collaboration et al. \(2024\)](#)), fluence-ratio draws are restricted to the absolute meridian angle $< 1^\circ$ subsample.

The injection-based selection function is evaluated in four dimensional space ([K. McGregor et al. 2026](#)), $S_4(F_\nu, DM_{\text{tot}}, W, \tau_{600})$, where F_ν is the injection fluence, DM_{tot} is the total dispersion measure, W is the pulse width, and τ_{600} is the scattering time. We also use the marginal fluence-only projection, denoted as $S_F(F_\nu)$, for the z - E visualization and for the synthetic-catalog filtering in the independence and forward tests. To remain within the fluence range where the pipeline completeness is better constrained, only baseband-like fluences in the range $5 \leq F_\nu \leq 200$ Jy ms are retained ([M. Merryfield et al. 2023](#); [K. McGregor et al. 2026](#)). After applying this draw-level cut, a typical catalog realization contains approximately 1300 events.

2.3. Backward Weighted Lynden-Bell C^- method

The complexity of using CHIME FRBs is that the reported catalog fluence is only a lower limit and the indirect redshift estimation from DM is probabilistic, which both introduce significant uncertainty in the redshift and energy estimation. To fully account for these uncertainties, a Monte Carlo approach is adopted to infer intrinsic distributions. Throughout this work, a draw denotes a single sampled latent quantity, such as a redshift or fluence-ratio value for one burst. A catalog realization denotes one Monte Carlo instantiation of the latent redshifts, fluence ratios, and energies for all selected CHIME/FRB Catalog 2 events. By contrast, a synthetic catalog denotes a forward-simulated FRB population drawn from an assumed intrinsic distribution and filtered through the survey selection function. To fully consider these uncertainties in an overall and robust sense, the following Monte Carlo procedure is utilized:

1. For each FRB, a latent redshift draw is sampled from its associated Gaussian distribution $z \sim \mathcal{N}(\mu_z, \sigma_z)$, and a baseband-to-catalog fluence-ratio draw is sampled to compute the corresponding energy draw E . The details of redshift and energy estimation are described in Appendix A ⁴.

⁴ We use Planck 2018 cosmology parameters ([Planck Collaboration et al. 2020](#)) in this work for comparison with previous studies, but since FRBs are local Universe phenomena and are mostly at $z \lesssim 2$, SH0ES cosmology parameters should be chosen. Therefore, we test using the SH0ES cosmology parameters from [A. G. Riess et al. \(2022\)](#) and found no significant difference for the result.

2. We repeat this sampling 1,000 times per event, generating an ensemble of 1,000 catalog realizations.
3. For each of these 1,000 catalog realizations, we apply the weighted Lynden-Bell method to derive an independent cumulative distribution for both redshift and energy.

We use the weighted Lynden-Bell C^- method to infer the intrinsic redshift and energy distributions of FRBs ([D. Lynden-Bell 1971](#)). This approach extends the classical non-parametric Lynden-Bell estimator by incorporating the fuzzy four dimensional selection function.

For redshift, the comparable set ([D. Lynden-Bell 1971](#); [B. Efron & V. Petrosian 1992](#)) is defined as

$$J_{z_i} = \{j : z_j \leq z_i, E_j \geq E(F_{\nu,\text{th}}, z_i)\}, \quad (1)$$

as illustrated by the green dashed boundary in Figure 2.

For energy, the comparable set is defined as

$$J_{E_i} = \{j : E_j \geq E_i, z_j \leq z(F_{\nu,\text{th}}, E_i)\}, \quad (2)$$

as illustrated by the purple dashed boundary in Figure 2.

Here, $E(F_{\nu,\text{th}}, z_i)$ and $z(F_{\nu,\text{th}}, E_i)$ describe the same fluence-limited boundary at $F_{\nu,\text{th}} = 5$ Jy ms. Notice that $F_{\nu,\text{th}}$ is not treated as a hard cutoff selection function like in previous non-parametric methods, but as a lower fluence boundary used to avoid CHIME pipeline noise misclassification ([M. Merryfield et al. 2023](#); [K. McGregor et al. 2026](#)). $E(F_{\nu,\text{th}}, z_i)$ is the minimum energy at redshift z_i corresponding to this fluence boundary, and $z(F_{\nu,\text{th}}, E_i)$ is the maximum redshift for a burst of energy E_i at this fluence boundary. Therefore, J_{z_i} compares events bright enough to be observed at z_i , whereas J_{E_i} compares events close enough to be observed at fixed E_i . $E(F_{\nu,\text{th}}, z_i)$ and $z(F_{\nu,\text{th}}, E_i)$ extend the original selection boundary $\{j : E_j \geq E_i, z_j \leq z_i\}$, make use of more data points, and give a more accurate estimation of the intrinsic distribution.

Let $F_\nu(z, E)$ be the baseband-like fluence corresponding to a burst with redshift z and energy E . Equation (8) of [D. Lynden-Bell \(1971\)](#) is written in discrete weighted form as

$$C^-(z_i) = \sum_{j \in J_{z_i}} \frac{S_4[F_\nu(z_i, E_j), DM_{j \rightarrow i}, W_j, \tau_{600,j}]}{S_4[F_\nu(z_j, E_j), DM_{\text{tot},j}, W_j, \tau_{600,j}]} - 1 \quad (3)$$

where S_4 is the four dimensional selection function defined in Section 2.2. The denominator is the selection probability of event j at its observed coordinates. The numerator evaluates the same event after moving it to the trial redshift z_i while keeping E_j , W_j , and $\tau_{600,j}$ fixed. The shifted total DM is defined as $DM_{j \rightarrow i} = DM_{\text{tot},j} + 831(z_i - z_j)$, where 831 is the slope of

the median $\text{DM}_{\text{ext}-z}$ relation used in Appendix A. This shift keeps the event-specific DM residual fixed while evaluating the selection probability at the trial redshift. If setting $S_4 \equiv 1$, this method reduces to the original C^- method, which actually belongs to the general survival-analysis Kaplan–Meier estimator in statistics.

The inverse denominator is the weight of each event j in the comparable set, which accounts for the fact that events with lower detection probability should be weighted more heavily. The numerator accounts for the fact that the actual detected events at the infinitesimal redshift bin around z_i are the intrinsic events at this redshift bin multiplied by the selection function at this redshift bin. The -1 is to exclude the event i itself from the comparable set, which is the same trick as the original C^- method. The cumulative redshift distribution is therefore

$$P(z_i) = \int_{\leq z_i} p(z) dz = \prod_{j \leq i} \left(\frac{C_z^-(z_j) + 1}{C_z^-(z_j)} \right) \quad (4)$$

where $p(z)$ is the redshift probability density function. The cumulative distribution is a product of the contributions from each C^- of each event.

Applying the same procedure in energy space, we obtain

$$C_E^-(E_i) = \sum_{j \in J_{E_i}} \frac{S_4[F_\nu(z_j, E_i), \text{DM}_{\text{tot},j}, W_j, \tau_{600,j}]}{S_4[F_\nu(z_j, E_j), \text{DM}_{\text{tot},j}, W_j, \tau_{600,j}]} - 1 \quad (5)$$

In this case the trial energy changes the fluence of event j , but the redshift, total DM, width, and scattering time are fixed at the observed values.

The corresponding cumulative energy distribution is

$$\Psi(E_i) = \int_{\geq E_i} \psi(E) dE = \prod_{j \leq i} \left(\frac{C_E^-(E_j)}{C_E^-(E_j) + 1} \right) \quad (6)$$

where $\psi(E)$ is the energy probability density function. The cumulative distribution is a product of the contributions from each C^- of each event.

2.4. Simulation-based redshift–energy independence test

The Lynden–Bell C^- method assumes statistical independence between redshift and energy (D. Lynden–Bell 1971). Under this assumption, the redshift and energy distributions can be inferred as separate marginal distributions, but the joint redshift–energy distribution is not directly recovered. The same pair of marginal distributions can be projection from many joint distributions with different redshift–energy correlation structures. Testing redshift–energy independence is therefore necessary both for interpreting the physical origin of FRBs and for assessing whether the C^- framework is self-consistent for this application.

Although B. Efron & V. Petrosian (1992) developed a non-parametric independence test for samples with a sharp truncation boundary, no direct analogue is available for the fuzzy selection function used here. In the weighted comparable sets, each data point carries a selection-dependent weight, so the rank structure assumed by the standard test is no longer preserved. A simulation-based independence test is therefore adopted:

1. For each catalog realization, the intrinsic redshift and energy marginal distributions are inferred with the weighted Lynden–Bell C^- method (see Section 2.3).
2. Intrinsic synthetic catalogs are generated by independently drawing redshift and energy values from the inferred marginal distributions.
3. The marginal fluence selection function is applied to each synthetic catalog.
4. The observed and synthetic samples are restricted to the same redshift and energy ranges.
5. Pearson, Spearman, and Kendall correlation statistics are compared between the catalog realizations and the synthetic catalogs.

Under independence, the catalog realizations’s correlation coefficients should overlap with synthetic catalogs.

2.5. Forward population synthesis method

Monte Carlo population synthesis provides an independent forward constraint on the intrinsic FRB population by testing candidate redshift and energy distributions directly against the observed extragalactic dispersion measure and fluence distributions. The main procedure follows standard FRB population-synthesis approaches (R. C. Zhang et al. 2021; R. C. Zhang & B. Zhang 2022; D.-C. Qiang et al. 2022; Z.-L. Zhang et al. 2023) and is implemented as follows:

1. A synthetic catalog is generated by drawing redshift and energy pairs, (z, E) , from the intrinsic probability density functions.
2. For each synthetic event, the baseband-like fluence F_ν is calculated from its drawn energy and redshift. The synthetic events are then filtered through the marginal fluence selection function described in Section 2.2.
3. For each selected synthetic event, an extragalactic dispersion measure is drawn from the extrapolated DM_{ext} –redshift relation derived by J. Zhuge et al. (2026). We write the median relation and its empirical upper 1σ linear offset as $\mu_{\text{DM}}(z) = 831z + 111$ and $\sigma_{\text{DM}}(z) = 59z + 155$, in units of pc cm^{-3} . To account for uncertainty in this relation, DM_{ext}

at fixed redshift is drawn from a log-normal distribution, which preserves the non-negative physical boundary and allows a long high- DM_{ext} tail from line-of-sight density fluctuations (M. McQuinn 2014; J. P. Macquart et al. 2020). The draw is implemented with `numpy.random.lognormal`.

4. For each catalog realization, baseband-like fluences are recomputed by drawing a fresh baseband-to-catalog fluence ratio for each observed FRB from the same empirical distribution used in Section 2.3. These fluence-ratio draws are independent of those used in the backward inference.
5. Each catalog realization is compared with each selected synthetic catalog using two-sample Kolmogorov–Smirnov (KS) tests applied separately to the DM_{ext} and baseband-like fluence distributions.

3. RESULTS

3.1. Marginal redshift and energy distribution

The cumulative redshift distributions inferred from the 1,000 CHIME/FRB Catalog 2 realizations are shown by the gray solid curves in the upper panel of Figure 3. The corresponding probability density function is shown by the gray solid histogram in the lower panel. The inferred redshift distribution peaks near $z \sim 1$, below the SFH peak at $z \sim 1.7$. In both panels, the inferred distribution departs substantially from the SFH model and is closer to delayed population models. Details of the model redshift distributions are given in Appendix B. The stellar mass density model (orange dashed curve) lies within the uncertainty region. The representative delayed models shown in Figure 3 include a log-normal delay time distribution with $\tau_{\text{LN}} = 5$ Gyr and $\sigma_{\text{LN}} = 1$, and a power-law delay time distribution with $\tau_c = 5$ Gyr. These comparisons are intended as qualitative visualization rather than formal best fits, because the inferred redshift distribution remains affected by uncertainties in both the $z(\text{DM}_{\text{ext}})$ relation and the empirical baseband-to-catalog fluence-ratio correction. The models are therefore used only to assess whether the recovered distribution is closer to prompt SFH tracking or to broadly delayed evolutionary histories. As an additional check on the fluence-ratio correction, Appendix C presents the marginal redshift distribution inferred from the baseband catalog, for which fluences are directly measured. Its agreement with the weighted Catalog 2 inference supports the use of the empirical fluence-ratio correction.

The cumulative energy distribution is shown in Figure 4. No distinct feature is found near $E \sim 10^{39}$ erg. Assuming a power-law probability density, $\psi \propto E^{-\alpha}$, the inferred slope is $\alpha \approx 1.9$ below 10^{42} erg. The distribution steepens, broadly consistent with previous studies

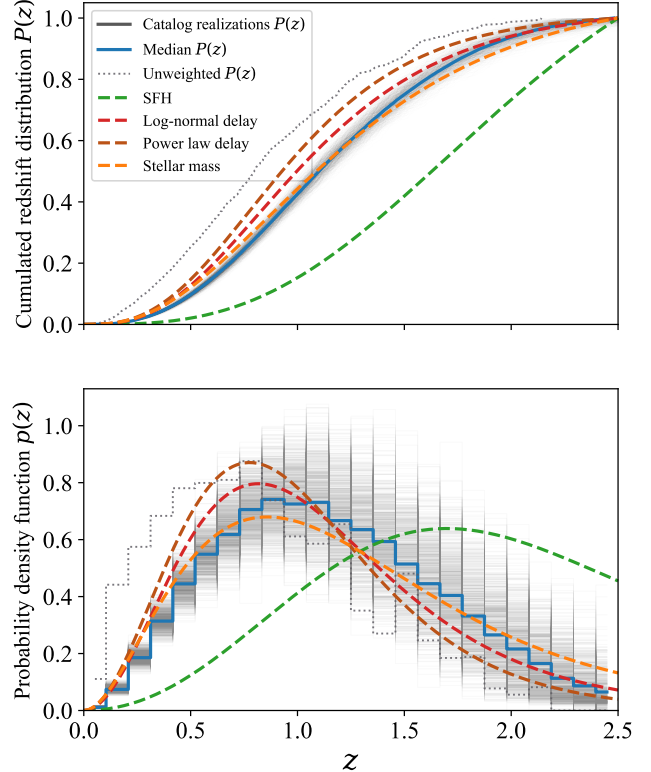


Figure 3. Redshift distribution functions. Upper panel: cumulative distribution functions. Gray solid curves show the cumulative distributions derived from the 1,000 catalog realizations, and the blue solid curve shows their median. The green dashed curve denotes the SFH model; the red dashed curve denotes a delayed star-formation model with a log-normal delay time distribution with $\tau_{\text{LN}} = 5$ Gyr and $\sigma_{\text{LN}} = 1$; the brown dashed curve denotes a delayed star-formation model with a power-law delay time distribution with $\tau_c = 5$ Gyr; and the orange dashed curve denotes the stellar mass density model. The gray dashed curve shows the unweighted C^- result obtained using the original catalog fluence, without the baseband-to-catalog fluence-ratio corrections. Lower panel: probability density functions. The same color scheme is used as in the upper panel. The gray solid histogram shows the probability density function derived from the weighted catalog realizations, while the gray dashed histogram shows the corresponding unweighted result.

(e.g., R. Luo et al. 2020; T. Hashimoto et al. 2022; K. Shin et al. 2023).

Setting the selection function to unity recovers the unweighted original C^- estimator. For comparison with previous unweighted results (e.g., J. H. Chen et al. 2024; K. J. Zhang et al. 2025; S. Champati & V. Petrosian 2025), the baseband-to-catalog fluence ratio is also fixed to unity and the redshift is only the median value of $\text{DM}_{\text{ext}}-z$ relation without propagating its probability

distribution. The corresponding redshift results are shown by the gray dashed curve and histogram in Figure 3, while the corresponding energy results are shown by the gray points in Figure 4. The unweighted inference yields a more delayed redshift distribution than the weighted cases and a shallower energy slope of approximately $\alpha \approx 1.6$.

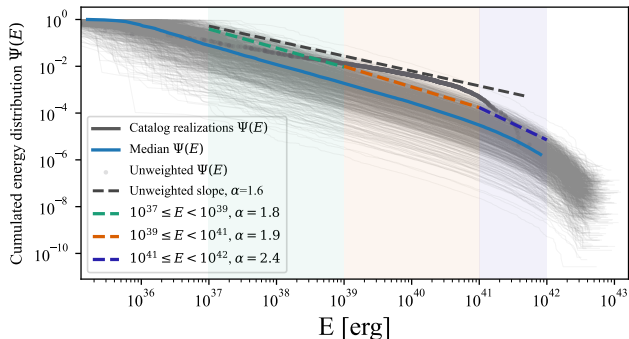


Figure 4. Cumulative energy distribution functions. Gray solid curves show the cumulative distributions derived from the 1,000 catalog realizations, and the blue solid curve shows their median. α denotes the slope of the power-law energy probability density function, $\psi \propto E^{-\alpha}$. Dashed lines show piecewise power-law fits to the cumulative distribution, with different segments indicated by different colors. Gray points show results from the unweighted original C^- estimator with the original catalog fluence, which yields a shallower slope.

3.2. Redshift–energy independence test

Although the inferred energy distribution shown in Figure 4 spans approximately 10^{35} – 10^{43} erg, the low-energy tail below 10^{37} erg is constrained by relatively few data points. We therefore impose $E_{\min} = 10^{37}$ erg in the independence-test simulations, restricting the synthetic draws to the energy range where the inferred distribution is more densely sampled and more stable. This lower energy cut also reduces the computational cost of sampling a distribution that spans many orders of magnitude. For each independence-test realization, 3×10^6 intrinsic synthetic FRB events are generated. After the marginal fluence selection function is applied, this choice yields approximately 1300 detectable events, comparable to the final observed sample size.

A total of 1000 independence-test realizations are generated under the redshift–energy independence assumption. Pearson, Spearman, and Kendall correlation coefficients⁵ are evaluated for each realization. The resulting distributions are shown in Figure 5; solid histograms denote the catalog realizations, and dashed histograms denote the synthetic catalogs generated un-

der the independence assumption. For all three statistics, the catalog–realization distributions overlap substantially with the corresponding synthetic–catalog distributions. This agreement indicates that the data do not provide significant evidence for an intrinsic redshift–energy distribution correlation after accounting for the selection function and the baseband-to-catalog fluence correction.

The unweighted comparison is constructed by setting the selection function to unity, fixing the baseband-to-catalog fluence ratio to unity, and assigning each burst the median redshift from the $DM_{\text{ext}}-z$ relation without propagating the redshift-probability distribution (e.g., J. H. Chen et al. 2024; K. J. Zhang et al. 2025; S. Champati & V. Petrosian 2025). The catalog correlation coefficients for this unweighted case are shown by gray vertical lines, while the corresponding independence-test distributions from 1000 synthetic catalogs are shown by gray dashed histograms. The gray vertical lines are clearly displaced from the corresponding gray histograms, indicating a strong apparent redshift–energy correlation in the unweighted case. This apparent correlation is likely induced by selection effects (C. M. Bryant et al. 2021), because the unweighted estimator does not account for the fuzzy selection function and treats the catalog-reported fluence, which is generally a lower limit, as the intrinsic fluence.

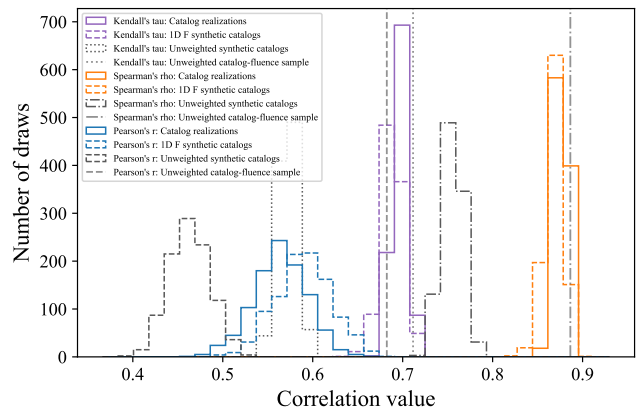


Figure 5. Correlation coefficients between redshift and energy. Solid histograms show the coefficient distributions from the catalog realizations. Dashed histograms show the corresponding distributions from 1000 synthetic catalogs generated under the redshift–energy independence assumption and passed through the marginal fluence selection function. Gray vertical lines show the median coefficients from the unweighted inference with the original catalog fluence, and gray dashed histograms show the corresponding unweighted synthetic–catalog distributions.

⁵ Computed with `scipy.stats` (P. Virtanen et al. 2020).

3.3. Forward population synthesis

Monte Carlo population synthesis is used as an independent forward constraint on the population. DM_{ext} and fluence distributions are the final observables in Catalog 2, whereas redshift and energy are inferred variables. Therefore, candidate intrinsic redshift and energy distributions can be constrained by comparing the DM_{ext} and fluence distributions from the forward simulation with the observed DM_{ext} and fluence distributions. To ensure a fair comparison with observations, each synthetic catalog realization is truncated using the same observed ranges in DM_{ext} and baseband-like fluence (minimum and maximum values). The resulting DM_{ext} and baseband-like fluence distributions are then compared with the observed distributions.

Figure 6 compares the weighted Lynden–Bell result from CHIME/FRB Catalog 2 with representative models using the same parameter choices as in Figure 3. The SFH model (dash green histogram) predicts a DM_{ext} distribution peaked at higher DM_{ext} than the observed distribution, while the delayed models are more consistent with the observed distribution.

Because individual synthetic-catalog realizations can fluctuate, stability is assessed from the distribution of KS test p -values of each catalog realization versus each synthetic catalog rather than from a single run. All models can pass the KS test for baseband-like fluence, but the delayed models are more likely to pass. The KS test p -value for the SFH model in DM_{ext} is $\sim 10^{-30}$, indicating strong tension with the observed DM_{ext} distribution across synthetic-catalog realizations (Figure 7).

The reproduction of the DM_{ext} and fluence distribution therefore provides an independent consistency check of the redshift and energy distribution.

4. SUMMARY AND DISCUSSION

In this work, we apply a backward weighted Lynden–Bell C^- framework to the CHIME/FRB Catalog 2, explicitly using survey selection effects through an injection-based multidimensional selection function. Redshift and energy distribution independence is tested with a simulation-based approach. An independent forward population synthesis is also used to constrain candidate intrinsic population models against final observables. By combining this weighted non-parametric inference with forward modeling, we first provide a self-consistent demographic description of the Catalog 2 population. Crucially, our dual-methodology approach is designed to be both concise and robust: it intentionally avoids introducing excessive complexity, free parameters, or model assumptions, while strictly preserving the proper rigor required to account for complex observational selection biases.

The main results are summarized as follows.

1. The redshift distribution peaks near $z \sim 1$ and deviates from a pure SFH (SFH peak near $z \sim$

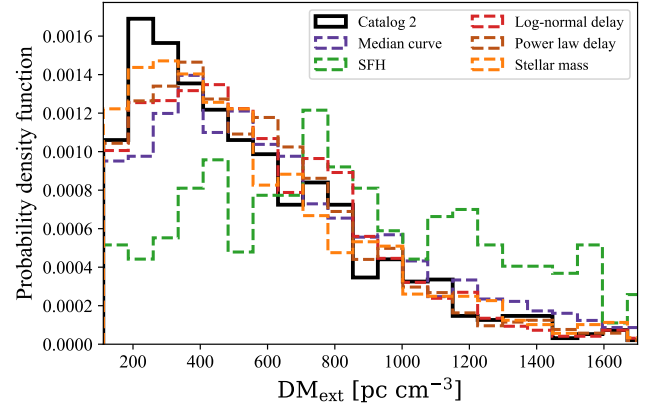


Figure 6. DM_{ext} distribution. The same color scheme is used as in Figure 3, except that the CHIME Catalog 2 DM_{ext} distribution is shown by the solid black histogram. For each detectable synthetic event, DM_{ext} is assigned using $DM_{\text{ext}}(z)$ distribution and the same DM_{ext} selection in Section 2.1 is applied. Notice that the x-axis is linear, while in K. Shin et al. (2023); CHIME/FRB Collaboration et al. (2026), the x-axis is logarithmic. There is transformation between linear scale and logarithmic scale for probability density function, which is $p(x) = p(\log x)/x$. The linear scale is more intuitive for DM_{ext} distribution, since DM_{ext} is a linear proxy of redshift.

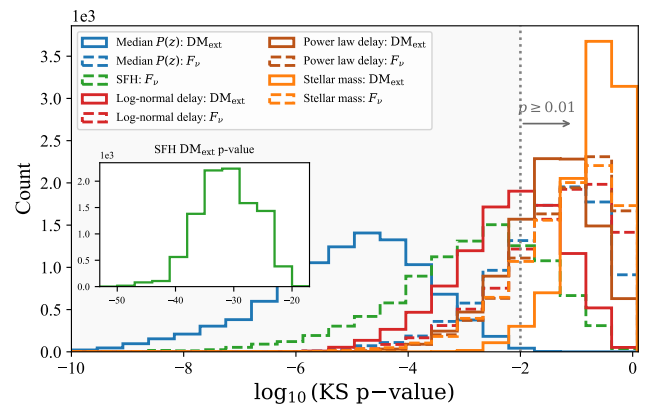


Figure 7. Kolmogorov–Smirnov test p -values for DM_{ext} and F_ν . Same color scheme is used as in Figure 3. The solid histograms show the distribution of p -values of DM_{ext} . The dashed histograms show the distribution of p -values of baseband-like fluence. The zoom-in panel shows the p -value distribution of DM_{ext} .

1.7). The inferred shape is more consistent with delayed-population models than with SFH evolution.

2. A power-law behavior is found below 10^{42} erg with slope $\alpha \approx 1.9$, followed by a steepening.

3. A simulation-based independence test in the redshift–energy plane (1000 realizations) shows that the Pearson, Spearman, and Kendall coefficients of catalog realizations largely overlap with the synthetic-catalog distributions, supporting consistency with the redshift–energy independence.
4. Taking the $DM_{\text{ext}}(z)$ probability distribution into consideration, forward population synthesis in observable space also indicates strong tension between the SFH model and the observed DM_{ext} distribution (typical KS-test $p \sim 10^{-30}$).

Both the backward weighted Lynden–Bell inference of the intrinsic redshift distribution and the forward population synthesis of the observed DM_{ext} distribution independently confirm that the CHIME/FRB Catalog 2 population is delayed relative to the SFH. This self-consistent result aligns with previous demographic studies utilizing various methods and earlier samples (e.g., R. C. Zhang & B. Zhang 2022; T. Hashimoto et al. 2022; D.-C. Qiang et al. 2022; Z.-L. Zhang et al. 2023; J. H. Chen et al. 2024; K. J. Zhang et al. 2025; O. Gupta et al. 2025).

Explicitly incorporating the fuzzy survey selection function into the Lynden–Bell framework resolves several biases present in previous non-parametric studies. Compared to the weighted method, unweighted inference yields a redshift distribution that is notably more delayed. Moreover, the weighted method does not recover a significant redshift–energy correlation, demonstrating the critical importance of considering selection effects in FRB demographics.

Several methodological caveats should be noted. First, the baseband-to-catalog fluence ratio is sampled from an empirical distribution, but its possible dependence on other observables, such as pulse width and scattering time, is not yet fully characterized. As a consistency check, Appendix C applies the weighted Lynden–Bell method directly to the baseband catalog, where fluences are better measured. The agreement between the Catalog 2 inference and the baseband-catalog inference supports the empirical fluence-ratio correction. Second, the backward Lynden–Bell weights use the four dimensional injection-based selection function, whereas the independence test and the forward-synthesis filtering use the marginal fluence selection function. This lower dimensional treatment reduces the assumptions and free parameters needed to model the dispersion-measure, pulse-width, and scattering-time distributions, but it may leave residual selection biases because the CHIME/FRB detection efficiency is coupled across fluence, dispersion measure, pulse width, and scattering time (K. McGregor et al. 2026). Appendix C also applies the marginal fluence selection function to the baseband sample. The resulting redshift distribution is

consistent with the inference based on the four dimensional selection function, suggesting that the marginal fluence approximation is qualitatively adequate. Third, the backward inference approximates the redshift uncertainty as Gaussian, which may affect the recovered intrinsic redshift distribution. Finally, the energy estimate in Equation A3 carries an implicit spectral assumption: it treats the relevant energy scale as a band-averaged CHIME-band quantity, appropriate if bursts are effectively narrowband or if the event rate does not vary strongly across the observing frequencies considered here. Appendix D examines the alternative case in which FRBs are broadband sources with a frequency-dependent spectrum. Unless the FRB occurrence rate is strongly frequency dependent, or the spectral index is extremely steep, this test indicates that the main redshift-distribution conclusion is not qualitatively changed.

The inferred delay relative to the SFH is consistent with the existence of FRBs in old stellar environments, including globular clusters and early-type galaxies (e.g., M. Bhardwaj et al. 2021; T. Eftekhari et al. 2025), and with the finding that FRB host-galaxy properties occupy an intermediate regime between long-GRB hosts, which more closely trace star formation, and short-GRB hosts, which are more delayed (Y. Li & B. Zhang 2020). At the same time, some FRBs, especially active repeaters, are associated with star-forming environments (e.g., S. P. Tendulkar et al. 2017; B. Marcote et al. 2020; C.-H. Niu et al. 2022; H. Xu et al. 2022). A mixed population is therefore more plausible than a single progenitor channel. Because this work focuses on apparent non-repeaters, the results suggest that this subsample is more delayed than the active-repeater population. In a magnetar framework, this trend would be consistent with a decline in FRB activity with source age. It could also indicate additional engines or triggering channels whose rates do not closely follow the SFH. A larger sample of precisely localized FRBs will be required to distinguish these possibilities.

ACKNOWLEDGMENTS

We thank Matthew Bailes, Vicky Kaspi, and Kaitlyn Shin for helpful comments. Z.Z. is deeply grateful to Yi-Han Iris Yin for exceptionally insightful discussions on the key ideas of the Lynden–Bell method. Z.Z. also thanks Jiaming Zhuge for helpful discussions and for sharing code related to the $DM-z$ relation and its uncertainty distribution. AI-assisted tools (Codex and Gemini) were used by Z.Z. to support coding, code checking, and language polishing. Z.Z. reviewed and edited all AI-assisted outputs and takes full responsibility for the manuscript content, analyses, conclusions, code, and any remaining errors. This research has made use of NASA’s Astrophysics Data System (ADS). The

code used in this work is available from the authors upon reasonable request.

Software: Astropy (Astropy Collaboration et al. 2022), NumPy (C. R. Harris et al. 2020), Matplotlib (J. D. Hunter 2007), SciPy (P. Virtanen et al. 2020), tqdm (C. da Costa-Luis et al. 2024)

APPENDIX

A. REDSHIFT AND ENERGY ESTIMATION

The observed dispersion measure DM_{obs} of an FRB can be decomposed into Galactic and extragalactic components (e.g., D. Thornton et al. 2013; W. Deng & B. Zhang 2014):

$$DM_{\text{obs}} = DM_{\text{MW,ISM}} + DM_{\text{MW,halo}} + DM_{\text{ext}}, \quad (\text{A1})$$

and

$$DM_{\text{ext}} = DM_{\text{diff}} + \frac{DM_{\text{host}}}{1+z}. \quad (\text{A2})$$

Here, $DM_{\text{MW,ISM}}$ is the Milky Way interstellar medium contribution (estimated using the YMW16 model; J. M. Yao et al. 2017). $DM_{\text{MW,halo}}$ is the Milky Way halo contribution and 30 pc cm^{-3} is adopted in this work (e.g., K. Dolag et al. 2015), whose uncertainty is negligible, compared to other contributions. The extragalactic term DM_{ext} consists of the diffuse intergalactic medium and intervening halo contributions DM_{diff} , plus the redshift diluted contribution from the FRB host galaxy DM_{host} .

To estimate the pseudo redshift, we extrapolate the empirical median $DM_{\text{ext}}-z$ relation derived from localized FRBs (J. Zhuge et al. 2026) to the range $z \in (0, 3)$: $\mu_z = \frac{DM_{\text{ext}}/(\text{pc cm}^{-3}) - 111}{831}$. Physically, the probability distribution of DM_{ext} at a fixed redshift is approximately log-normal, exhibiting a long tail toward high DM values (e.g., M. McQuinn 2014; J. P. Macquart et al. 2020; Z. J. Zhang et al. 2021). Consequently, the inverse redshift distribution at a fixed DM_{ext} possesses a long tail toward low redshifts and lacks a simple analytical form. For computational tractability in our framework, we approximate this inverse distribution as a Gaussian, $z \sim \mathcal{N}(\mu_z(DM_{\text{ext}}), \sigma_z(DM_{\text{ext}}))$. We define the 1σ redshift uncertainty using an empirical linear approximation: $\sigma_z \approx 8 \times 10^{-5} \left(\frac{DM_{\text{ext}}}{\text{pc cm}^{-3}} \right) + 0.17$. While this symmetric Gaussian approximation likely underestimates the low-redshift tail and overestimates the high-redshift uncertainty, it provides a practical metric for error propagation. For low DM_{ext} events, a positive-only truncated Gaussian is used to avoid negative redshift.

The isotropic equivalent energy of each FRB is then calculated following:

$$E = \frac{1}{1+z} 4\pi d_L^2 F_\nu \Delta\nu, \quad (\text{A3})$$

where d_L is the luminosity distance assuming Planck 2018 cosmology (Planck Collaboration et al. 2020), F_ν

is the baseband like fluence, and $\Delta\nu = 400 \text{ MHz}$ is the bandwidth of the CHIME band, since reported fluence is averaged over this bandwidth (CHIME/FRB Collaboration et al. 2021). Using $\Delta\nu$ rather than the central frequency ν_c to calculate FRB energy is more appropriate for FRBs with a relatively narrow spectrum (B. Zhang 2023). Most of the bursts in the CHIME/FRB Catalog 2 are detected with a peak narrow band spectrum (CHIME/FRB Collaboration et al. 2026), some bursts are detected with an increasing spectrum and some bursts are detected with a decreasing spectrum. The uncertainty in the derived energy is dominated by the baseband-catalog fluence and redshift estimation, this energy estimation is parameterless and model-independent.

B. REDSHIFT DISTRIBUTION MODELS

To physically interpret the inferred FRB redshift distribution, the results are compared against theoretical population models.

The cosmic star-formation history parameterized by P. Madau & M. Dickinson (2014) is adopted. The pure cosmic star-formation history model assumes the FRB event rate directly tracks the star-formation rate without delay, which is characteristic of young progenitor systems (e.g., magnetars born from core-collapse supernovae). Furthermore, the stellar mass density model (Equation 2 of P. Madau & M. Dickinson 2014) is considered, which assumes the FRB rate is proportional to the total accumulated stellar mass in the Universe, representative of very old stellar populations.

Delayed models account for the evolutionary timescale between the formation of the progenitor system and the subsequent FRB event. The delayed comoving FRB event-rate density (events per unit time per unit volume) can be written as the convolution of the star-formation rate with a delay time distribution (e.g., X.-J. Zhu et al. 2013; D. Wanderman & T. Piran 2015; X.-F. Cao et al. 2018):

$$\dot{R}(z) \propto (1+z) \int_0^{t(z)-t_b} \frac{\dot{\rho}_*[t(z)-\tau]}{1+z[t(z)-\tau]} P(\tau) d\tau, \quad (\text{B4})$$

where $\dot{\rho}_*$ is the cosmic star formation rate, $P(\tau)$ is the delay time distribution, and τ is the delay time. Equivalently, integrated over redshift, this becomes:

$$\dot{R}(z) \propto (1+z) \int_z^{z_b} \frac{\dot{\rho}_*(z')}{1+z'} P[t(z)-t(z')] \left| \frac{dt}{dz'} \right| dz'. \quad (\text{B5})$$

The maximum redshift of star formation is set to $z_b = 10$. Because the cosmic star-formation rate drops rapidly at $z > 2$, the exact choice of z_b does not meaningfully affect the resulting convolution.

The delay time distribution, $P(\tau)$, characterizes the probability of a FRB event occurring at a given time τ after progenitor formation. This delay is modeled using two commonly adopted functional forms (e.g., [D. Wanderman & T. Piran 2015](#); [X.-F. Cao et al. 2018](#)):

(i) A log-normal function, defined as:

$$P(\tau) \propto \exp\left[-\frac{(\ln \tau - \ln \tau_{\text{LN}})^2}{2\sigma_{\text{LN}}^2}\right]. \quad (\text{B6})$$

(ii) A power-law function, defined as:

$$P(\tau) \propto \left(\frac{\tau}{\tau_c}\right)^{-1} \exp\left(-\frac{\tau_c}{\tau}\right). \quad (\text{B7})$$

Finally, to convert the comoving volume density to an observable redshift distribution, the probability density function is given by (e.g., [R. C. Zhang et al. 2021](#)):

$$p(z) \propto \dot{R}(z) \frac{dV_c}{dz} \frac{1}{1+z}, \quad (\text{B8})$$

where dV_c/dz is the comoving volume element per unit redshift, and the $1/(1+z)$ factor accounts for cosmological time dilation.

C. BASEBAND CATALOG CONSISTENCY CHECK

To test the empirical baseband-to-catalog fluence correction, the weighted Lynden–Bell C^- method is also applied directly to the original baseband catalog ([CHIME/FRB Collaboration et al. 2024](#)). The baseband catalog has much higher time resolution than Catalog 2, which can lead to different measured widths and scattering times for the same burst. For this reason, only the marginal fluence selection function, $S_F(F_\nu)$, is applied to the baseband sample. The same sample selection criteria as Section 2.1 are applied to ensure a consistent comparison.

The inferred redshift distribution is shown in Figure 8. It is consistent with four dimension selection main-text result, indicating that the empirical baseband-to-catalog fluence correction does not drive the inferred delayed redshift distribution and using marginal fluence selection does not introduce a significant difference.

D. VARYING SPECTRAL INDEX

The spectra of FRBs remain poorly constrained. There is evidence that non-repeating FRBs have wider observed bandwidths than repeating FRBs (e.g., [Z. Pleunis et al. 2021](#)). The CHIME sky rate at 600 MHz is $525 \text{ day}^{-1} \text{ sky}^{-1}$ above 5 Jy ms ([CHIME/FRB Collaboration et al. 2021](#)). After rescaling to the same fluence threshold with $N(> F_\nu) \propto F_\nu^{-1.5}$, the ASKAP

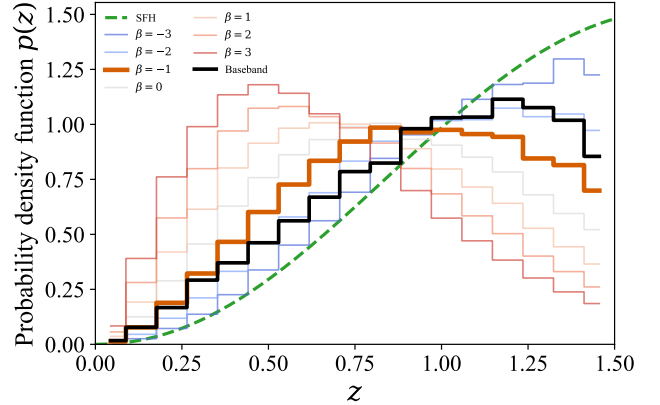


Figure 8. Redshift distribution functions from the baseband catalog and from tests with different spectral indices. The baseband-catalog result is shown by the black solid line. After applying the same sample selection as Section 2.1, 64 baseband bursts remain. The marginal fluence selection function is applied to the baseband catalog. Colored solid lines show the inferred redshift distributions for different spectral indices. The $\beta = -1$ case corresponds to the main-text result. The SFH model is shown by the dashed green curve. Because of the limited baseband sample size and for a fair comparison, all distributions are truncated at $z = 1.5$ and normalized by the area under the curve.

rate is $\sim 440 \text{ day}^{-1} \text{ sky}^{-1}$ at 1.3 GHz ([R. M. Shannon et al. 2018](#)) and the Parkes rate is $\sim 430 \text{ day}^{-1} \text{ sky}^{-1}$ at 1.4 GHz ([S. Bhandari et al. 2018](#)). These rates do not require an extremely steep frequency dependence of the burst occurrence rate. On the other hand, ultrawideband observations of the hyper-active repeater FRB 20240114A show extreme spectral variability and narrowband bursts also support a non-broadband interpretation for FRBs ([P. A. Uttarkar et al. 2026](#)). The intrinsic physical bandwidth of non-repeating FRBs is still unknown.

Over the 400 MHz CHIME band, there are two simple possible descriptions for non-repeating FRBs. First, the emission may be intrinsically narrowband, with a distribution of central frequencies determining which observing band each burst appears in. Second, the emission may be intrinsically broadband and approximated by a power-law spectrum. Although physically different, these two descriptions affect the inferred redshift distribution in a similar direction. If the event rate (for narrowband case) or rest-frame spectrum (for broadband case) declines strongly toward higher frequency, high-redshift bursts are observed at higher rest-frame frequencies and are more likely to be missed in a fixed observing band. Correcting for this effect would shift the inferred intrinsic redshift distribution toward higher redshift.

In this Appendix, we adopt the broadband interpretation as a diagnostic test and quantify how much the in-

ferred redshift distribution changes with spectral index. Including the K-correction, the energy is calculated as (N. Locatelli et al. 2019; C. W. James et al. 2022b; K. Shin et al. 2023)

$$E = \frac{1}{(1+z)^{2+\beta}} 4\pi d_L^2 F_\nu \Delta\nu, \quad (\text{D9})$$

where β is the spectral index of $F_\nu \propto \nu^\beta$. The case $\beta = -1$ reduces to the main-text energy definition (Equation A3); in the main analysis, Equation A3 is interpreted as a band-averaged, narrowband energy estimate over the CHIME band.

The effect of varying spectral index on the inferred redshift distribution is shown in Figure 8. Under the

broadband assumption, previous studies have suggested a characteristic spectral index of approximately $\beta \sim -1.5$ for non-repeating FRBs (J.-P. Macquart et al. 2019; K. Shin et al. 2023). Changing β shifts the inferred distribution in the expected direction, but it does not change the qualitative conclusion of this work over the range tested here. Unless the spectral index is extremely steep, the inferred redshift distribution remains inconsistent with the SFH model. For example, even for $\beta = -3$, the inferred distribution is still more consistent with a delayed model than with the SFH model. Therefore, uncertainty in the spectral index is not a dominant systematic factor for the main conclusion of this work.

REFERENCES

- Andersen, B. C., Patel, C., Brar, C., et al. 2023, *AJ*, 166, 138, doi: [10.3847/1538-3881/accc78](https://doi.org/10.3847/1538-3881/accc78)
- Astropy Collaboration, Price-Whelan, A. M., Lim, P. L., et al. 2022, *ApJ*, 935, 167, doi: [10.3847/1538-4357/ac7c74](https://doi.org/10.3847/1538-4357/ac7c74)
- Bannister, K. W., Deller, A. T., Phillips, C., et al. 2019, *Science*, 365, 565, doi: [10.1126/science.aaw5903](https://doi.org/10.1126/science.aaw5903)
- Bhandari, S., Keane, E. F., Barr, E. D., et al. 2018, *MNRAS*, 475, 1427, doi: [10.1093/mnras/stx3074](https://doi.org/10.1093/mnras/stx3074)
- Bhardwaj, M., Kirichenko, A. Y., Michilli, D., et al. 2021, *ApJL*, 919, L24, doi: [10.3847/2041-8213/ac223b](https://doi.org/10.3847/2041-8213/ac223b)
- Bochenek, C. D., Ravi, V., Belov, K. V., et al. 2020, *Nature*, 587, 59, doi: [10.1038/s41586-020-2872-x](https://doi.org/10.1038/s41586-020-2872-x)
- Bryant, C. M., Osborne, J. A., & Shahmoradi, A. 2021, *MNRAS*, 504, 4192, doi: [10.1093/mnras/stab1098](https://doi.org/10.1093/mnras/stab1098)
- Caleb, M., Flynn, C., Bailes, M., et al. 2016, *MNRAS*, 458, 708, doi: [10.1093/mnras/stw175](https://doi.org/10.1093/mnras/stw175)
- Cao, X.-F., Yu, Y.-W., & Zhou, X. 2018, *ApJ*, 858, 89, doi: [10.3847/1538-4357/aabadd](https://doi.org/10.3847/1538-4357/aabadd)
- Champati, S., & Petrosian, V. 2025, *ApJL*, 988, L64, doi: [10.3847/2041-8213/adefdb](https://doi.org/10.3847/2041-8213/adefdb)
- Chatterjee, S., Law, C. J., Wharton, R. S., et al. 2017, *Nature*, 541, 58, doi: [10.1038/nature20797](https://doi.org/10.1038/nature20797)
- Chen, J. H., Jia, X. D., Dong, X. F., & Wang, F. Y. 2024, *ApJL*, 973, L54, doi: [10.3847/2041-8213/ad7b39](https://doi.org/10.3847/2041-8213/ad7b39)
- CHIME/FRB Collaboration, Amiri, M., Bandura, K., et al. 2018, *ApJ*, 863, 48, doi: [10.3847/1538-4357/aad188](https://doi.org/10.3847/1538-4357/aad188)
- CHIME/FRB Collaboration, Andersen, B. C., Bandura, K. M., et al. 2020, *Nature*, 587, 54
- CHIME/FRB Collaboration, Amiri, M., Andersen, B. C., et al. 2021, *ApJS*, 257, 59, doi: [10.3847/1538-4365/ac33ab](https://doi.org/10.3847/1538-4365/ac33ab)
- CHIME/FRB Collaboration, Amiri, M., Andersen, B. C., et al. 2024, *ApJ*, 969, 145, doi: [10.3847/1538-4357/ad464b](https://doi.org/10.3847/1538-4357/ad464b)
- CHIME/FRB Collaboration, Abbott, T., Andersen, B. C., et al. 2026, *ApJS*, 283, 34, doi: [10.3847/1538-4365/ae3828](https://doi.org/10.3847/1538-4365/ae3828)
- da Costa-Luis, C., Aabdin, I., Alam, S., et al. 2024, *tqdm*: A Fast, Extensible Progress Bar for Python and CLI,, GitHub repository <https://github.com/tqdm/tqdm>
- Deng, W., & Zhang, B. 2014, *ApJL*, 783, L35, doi: [10.1088/2041-8205/783/2/L35](https://doi.org/10.1088/2041-8205/783/2/L35)
- Dolag, K., Gaensler, B. M., Beck, A. M., & Beck, M. C. 2015, *MNRAS*, 451, 4277, doi: [10.1093/mnras/stv1190](https://doi.org/10.1093/mnras/stv1190)
- Driessen, L. N., Barr, E. D., Buckley, D. A. H., et al. 2024, *MNRAS*, 527, 3659, doi: [10.1093/mnras/stad3329](https://doi.org/10.1093/mnras/stad3329)
- Efron, B., & Petrosian, V. 1992, *ApJ*, 399, 345, doi: [10.1086/171931](https://doi.org/10.1086/171931)
- Eftekhari, T., Dong, Y., Fong, W., et al. 2025, *ApJL*, 979, L22, doi: [10.3847/2041-8213/ad9de2](https://doi.org/10.3847/2041-8213/ad9de2)
- Gaensler, B. M. 2014, *GRB Coordinates Network*, 16533, 1
- Gupta, O., Beniamini, P., Kumar, P., & Finkelstein, S. L. 2025, *ApJ*, 986, 100, doi: [10.3847/1538-4357/add14c](https://doi.org/10.3847/1538-4357/add14c)
- Harris, C. R., Millman, K. J., van der Walt, S. J., et al. 2020, *Nature*, 585, 357, doi: [10.1038/s41586-020-2649-2](https://doi.org/10.1038/s41586-020-2649-2)
- Hashimoto, T., Goto, T., Chen, B. H., et al. 2022, *MNRAS*, 511, 1961, doi: [10.1093/mnras/stac065](https://doi.org/10.1093/mnras/stac065)
- Hunter, J. D. 2007, *Computing in Science & Engineering*, 9, 90, doi: [10.1109/MCSE.2007.55](https://doi.org/10.1109/MCSE.2007.55)
- James, C. W., Prochaska, J. X., Macquart, J. P., et al. 2022a, *MNRAS*, 510, L18, doi: [10.1093/mnras/rlab117](https://doi.org/10.1093/mnras/rlab117)
- James, C. W., Prochaska, J. X., Macquart, J.-P., et al. 2022b, *MNRAS*, 509, 4775, doi: [10.1093/mnras/stab3051](https://doi.org/10.1093/mnras/stab3051)
- Kirsten, F., Marcote, B., Nimmo, K., et al. 2022, *Nature*, 602, 585, doi: [10.1038/s41586-021-04354-w](https://doi.org/10.1038/s41586-021-04354-w)
- Kothes, R., Sun, X., Gaensler, B., & Reich, W. 2018, *ApJ*, 852, 54, doi: [10.3847/1538-4357/aa9e89](https://doi.org/10.3847/1538-4357/aa9e89)
- Li, C. K., Lin, L., Xiong, S. L., et al. 2021, *Nature Astronomy*, 5, 378, doi: [10.1038/s41550-021-01302-6](https://doi.org/10.1038/s41550-021-01302-6)

- Li, Y., & Zhang, B. 2020, *ApJL*, 899, L6, doi: [10.3847/2041-8213/aba907](https://doi.org/10.3847/2041-8213/aba907)
- Locatelli, N., Ronchi, M., Ghirlanda, G., & Ghisellini, G. 2019, *A&A*, 625, A109, doi: [10.1051/0004-6361/201834722](https://doi.org/10.1051/0004-6361/201834722)
- Lorimer, D. R., Bailes, M., McLaughlin, M. A., Narkevic, D. J., & Crawford, F. 2007, *Science*, 318, 777, doi: [10.1126/science.1147532](https://doi.org/10.1126/science.1147532)
- Lu, W., & Kumar, P. 2016, *MNRAS*, 461, L122, doi: [10.1093/mnrasl/slw113](https://doi.org/10.1093/mnrasl/slw113)
- Lu, W., & Piro, A. L. 2019, *ApJ*, 883, 40, doi: [10.3847/1538-4357/ab3796](https://doi.org/10.3847/1538-4357/ab3796)
- Luo, R., Lee, K., Lorimer, D. R., & Zhang, B. 2018, *MNRAS*, 481, 2320, doi: [10.1093/mnras/sty2364](https://doi.org/10.1093/mnras/sty2364)
- Luo, R., Men, Y., Lee, K., et al. 2020, *MNRAS*, 494, 665, doi: [10.1093/mnras/staa704](https://doi.org/10.1093/mnras/staa704)
- Lynden-Bell, D. 1971, *MNRAS*, 155, 95, doi: [10.1093/mnras/155.1.95](https://doi.org/10.1093/mnras/155.1.95)
- Macquart, J.-P., Shannon, R. M., Bannister, K. W., et al. 2019, *ApJL*, 872, L19, doi: [10.3847/2041-8213/ab03d6](https://doi.org/10.3847/2041-8213/ab03d6)
- Macquart, J. P., Prochaska, J. X., McQuinn, M., et al. 2020, *Nature*, 581, 391, doi: [10.1038/s41586-020-2300-2](https://doi.org/10.1038/s41586-020-2300-2)
- Madau, P., & Dickinson, M. 2014, *ARA&A*, 52, 415, doi: [10.1146/annurev-astro-081811-125615](https://doi.org/10.1146/annurev-astro-081811-125615)
- Marcote, B., Nimmo, K., Hessels, J. W. T., et al. 2020, *Nature*, 577, 190, doi: [10.1038/s41586-019-1866-z](https://doi.org/10.1038/s41586-019-1866-z)
- McGregor, K., Hessels, J. W. T., Kaspi, V. M., et al. 2026, arXiv e-prints, arXiv:2606.26334, doi: [10.48550/arXiv.2606.26334](https://doi.org/10.48550/arXiv.2606.26334)
- McQuinn, M. 2014, *ApJL*, 780, L33, doi: [10.1088/2041-8205/780/2/L33](https://doi.org/10.1088/2041-8205/780/2/L33)
- Merryfield, M., Tendulkar, S. P., Shin, K., et al. 2023, *AJ*, 165, 152, doi: [10.3847/1538-3881/ac9ab5](https://doi.org/10.3847/1538-3881/ac9ab5)
- Niu, C.-H., Aggarwal, K., Li, D., et al. 2022, *Nature*, doi: [10.1038/s41586-022-04755-5](https://doi.org/10.1038/s41586-022-04755-5)
- Petroff, E., Hessels, J. W. T., & Lorimer, D. R. 2022, *A&A Rv*, 30, 2, doi: [10.1007/s00159-022-00139-w](https://doi.org/10.1007/s00159-022-00139-w)
- Planck Collaboration, Aghanim, N., Akrami, Y., et al. 2020, *A&A*, 641, A6, doi: [10.1051/0004-6361/201833910](https://doi.org/10.1051/0004-6361/201833910)
- Pleunis, Z., Good, D. C., Kaspi, V. M., et al. 2021, *ApJ*, 923, 1, doi: [10.3847/1538-4357/ac33ac](https://doi.org/10.3847/1538-4357/ac33ac)
- Qiang, D.-C., Li, S.-L., & Wei, H. 2022, *JCAP*, 2022, 040, doi: [10.1088/1475-7516/2022/01/040](https://doi.org/10.1088/1475-7516/2022/01/040)
- Ravi, V., Catha, M., D'Addario, L., et al. 2019, *Nature*, 572, 352, doi: [10.1038/s41586-019-1389-7](https://doi.org/10.1038/s41586-019-1389-7)
- Riess, A. G., Yuan, W., Macri, L. M., et al. 2022, *ApJL*, 934, L7, doi: [10.3847/2041-8213/ac5c5b](https://doi.org/10.3847/2041-8213/ac5c5b)
- Shannon, R. M., Macquart, J.-P., Bannister, K. W., et al. 2018, *Nature*, 562, 386, doi: [10.1038/s41586-018-0588-y](https://doi.org/10.1038/s41586-018-0588-y)
- Shin, K., Masui, K. W., Bhardwaj, M., et al. 2023, *ApJ*, 944, 105, doi: [10.3847/1538-4357/acaf06](https://doi.org/10.3847/1538-4357/acaf06)
- Tendulkar, S. P., Bassa, C. G., Cordes, J. M., et al. 2017, *ApJL*, 834, L7, doi: [10.3847/2041-8213/834/2/L7](https://doi.org/10.3847/2041-8213/834/2/L7)
- Thornton, D., Stappers, B., Bailes, M., et al. 2013, *Science*, 341, 53, doi: [10.1126/science.1236789](https://doi.org/10.1126/science.1236789)
- Uttarkar, P. A., Shannon, R. M., Gourdji, K., et al. 2026, arXiv e-prints, arXiv:2602.16409, doi: [10.48550/arXiv.2602.16409](https://doi.org/10.48550/arXiv.2602.16409)
- Virtanen, P., Gommers, R., Oliphant, T. E., et al. 2020, *Nature Methods*, 17, 261, doi: [10.1038/s41592-019-0686-2](https://doi.org/10.1038/s41592-019-0686-2)
- Virtanen, P., Gommers, R., Oliphant, T. E., et al. 2020, *Nature Methods*, 17, 261, doi: [10.1038/s41592-019-0686-2](https://doi.org/10.1038/s41592-019-0686-2)
- Wanderman, D., & Piran, T. 2015, *MNRAS*, 448, 3026, doi: [10.1093/mnras/stv123](https://doi.org/10.1093/mnras/stv123)
- Wang, Y., & van Leeuwen, J. 2024, *A&A*, 690, A377, doi: [10.1051/0004-6361/202450673](https://doi.org/10.1051/0004-6361/202450673)
- Xu, H., Niu, J. R., Chen, P., et al. 2022, *Nature*, 609, 685, doi: [10.1038/s41586-022-05071-8](https://doi.org/10.1038/s41586-022-05071-8)
- Yao, J. M., Manchester, R. N., & Wang, N. 2017, *ApJ*, 835, 29, doi: [10.3847/1538-4357/835/1/29](https://doi.org/10.3847/1538-4357/835/1/29)
- Yu, Y.-W., Cheng, K.-S., Shiu, G., & Tye, H. 2014, *JCAP*, 2014, 040, doi: [10.1088/1475-7516/2014/11/040](https://doi.org/10.1088/1475-7516/2014/11/040)
- Zhang, B. 2023, *Reviews of Modern Physics*, 95, 035005, doi: [10.1103/RevModPhys.95.035005](https://doi.org/10.1103/RevModPhys.95.035005)
- Zhang, K. J., Zhang, Z. B., Rodin, A. E., et al. 2025, *A&A*, 698, A18, doi: [10.1051/0004-6361/202450727](https://doi.org/10.1051/0004-6361/202450727)
- Zhang, R. C., & Zhang, B. 2022, *The Astrophysical Journal Letters*, 924, L14, doi: [10.3847/2041-8213/ac46ad](https://doi.org/10.3847/2041-8213/ac46ad)
- Zhang, R. C., Zhang, B., Li, Y., & Lorimer, D. R. 2021, *MNRAS*, 501, 157, doi: [10.1093/mnras/staa3537](https://doi.org/10.1093/mnras/staa3537)
- Zhang, Z. J., Yan, K., Li, C. M., Zhang, G. Q., & Wang, F. Y. 2021, *ApJ*, 906, 49, doi: [10.3847/1538-4357/abceb9](https://doi.org/10.3847/1538-4357/abceb9)
- Zhang, Z.-L., Yu, Y.-W., & Cao, X.-F. 2023, *A&A*, 675, A66, doi: [10.1051/0004-6361/202245511](https://doi.org/10.1051/0004-6361/202245511)
- Zhou, P., Zhou, X., Chen, Y., et al. 2020, *ApJ*, 905, 99, doi: [10.3847/1538-4357/abc34a](https://doi.org/10.3847/1538-4357/abc34a)
- Zhu, X.-J., Howell, E. J., Blair, D. G., & Zhu, Z.-H. 2013, *Monthly Notices of the Royal Astronomical Society*, 431, 882, doi: [10.1093/mnras/stt207](https://doi.org/10.1093/mnras/stt207)
- Zhuge, J., Kalomenopoulos, M., & Zhang, B. 2026, *ApJ*, 996, 66, doi: [10.3847/1538-4357/ae1a6d](https://doi.org/10.3847/1538-4357/ae1a6d)